Radiation Physics and Chemistry 210 (2023) 111059

Contents lists available at ScienceDirect

Radiation Physics and Chemistry

journal homepage: www.elsevier.com/locate/radphyschem

# Physical, mechanical, optical, and gamma radiation shielding properties of the BaO-based glass system prepared by the melt-quench technique: A review

Ardiansyah Ardiansyah [a], Heryanto Heryanto [a], Bidayatul Armynah [a], Hassan Salah [b,c], Abdelmoneim Sulieman [d], David A. Bradley [e,f], Dahlang Tahir [a,*]

[a] Department of Physics, Hasanuddin University, Makassar, 90245, Indonesia
[b] INAYA Medical Collage, Nuclear Medicine Department, Riyadh, Saudi Arabia
[c] College of Medical Radiologic Science, Sudan University of Science and Technology, Khartoum, Sudan
[d] Department of Radiology and Medical Imaging Sciences, College of Applied Medical Sciences, Prince Sattam bin Abdulaziz University, P.O. Box 422, Alkharj, 11942, Saudi Arabia
[e] Centre for Nuclear and Radiation Physics, Department of Physics, University of Surrey, Guildford, United Kingdom
[f] Centre for Applied Physics and Radiation Technologies, School of Engineering and Technology, Sunway University, 47500, Bandar Sunway, Selangor, Malaysia

ARTICLE INFO

Handling Editor: Dr. Chris Chantler

*Keywords:*
Barium oxide
Melt-quench technique
Gamma-ray shielding
Physical properties
Mechanical properties
Optical properties

ABSTRACT

This article presents the physical, mechanical, optical, and radiation shielding properties of several articles discussing BaO-based glass systems prepared by the melt-quench technique. Specifically, the article discussed is an article that reports experimentally the effectiveness of BaO-based glass systems as shielding gamma-ray radiation at an energy of 0.662 MeV published since 2019. In addition, we also compare the theoretical effectiveness of several glass systems by recalculating using Phy- X/PSD based on the respective compositions reported by previous studies at several energies, namely: 0.284, 0.347, 0.662, 0.826, 1.173, 1.333, and 2.506 MeV. Based on the analysis, the $Bi_2O_3$–BaO–$B_2O_3$ glass system is the best in terms of absorbing radiation. But it still needs to be developed to get the best physical, mechanical, and optical properties. With this article, scholars can more easily determine the composition of a BaO-based glass system to be applied as a more effective and high-quality radiation shield.

## 1. Introduction

Photons are uncharged radiation that can ionize matter even at low energies, such as ultraviolet light, because low-energy photons can create dense ionization clusters. Low-energy photons can transfer most or all of their energy to matter and create secondary electrons, further enhancing ionization (Mohammad Rafiei et al., 2022a, 2022b). Then, high-energy photons such as gamma rays, apart from being able to ionize matter, also have very short wavelengths and have higher abilities than low-energy photons in terms of penetrating the material they are subjected to (Ardiansyah et al., 2022; Asal et al., 2021). Ionizing radiation can cause damage to the cell structure of living organisms it is subjected to because the energy is sufficient to remove electrons from atoms or ionize matter (Ardiansyah et al., 2022; Gharissah et al., 2022). Therefore, the widespread application of radiation technology in several fields, such as agriculture, power generation, medicine, research centers, and aerospace applications can cause severe problems in the surrounding environment (Akman et al., 2022; Echeweozo et al., 2021). The resulting problems include mutation, cancer, stillbirth, infertility, newborn children's physical and mental disorders (Echeweozo et al., 2021). To reduce or keep the radiation dose that hits the object not exceeding the threshold, the As Low as Reasonably Achievable (ALARA) principle is applied. The three principles contained in ALARA to protect the environment from the dangers of ionizing radiation are time, distance, and shielding (Kim and Tseren, 2020). Shielding is a material that absorbs incoming radiation so that the intensity of passing radiation changes to a safe level (Muhammad et al., 2022; Rahmat et al., 2023).

Until now, shielding continues to experience development, several types of shielding that always attract attention, namely concrete-based shielding (Ardiansyah et al., 2023), polymer (Almurayshid et al.,

* Corresponding author.
*E-mail address:* dtahir@fmipa.unhas.ac.id (D. Tahir).

https://doi.org/10.1016/j.radphyschem.2023.111059
Received 22 February 2023; Received in revised form 22 May 2023; Accepted 23 May 2023
Available online 24 May 2023

2021), steel (Aygün, 2020) and glass (Abdel-Wahed et al., 2020). Compared to other types of shielding, the development of glass-based radiation shields is one of the most popular types. The literature shows tellurite, phosphate, borate, silicate, germinate, and barite oxides are the most well-known oxide-based glass formers (El-Zaidia et al., 1985; Hampton et al., 1987, 1988; Sidkey et al., 2002). In the articles reported by (Abdel-Wahed et al., 2020; Kaur et al., 2016), barite oxide (BaO) can improve the quality of formed glass. The use of barium attracts attention because of its high density, low toxicity, low price, abundant availability in nature, and even the properties of the composite structure will be better by making the structure compact (Kaur et al., 2019).

Another factor that affects the properties of composite materials as radiation shields is the method of manufacture. The methods that have been widely used are constituents of a glass, sol-gel method, chemical vapor deposition (CVD), and melt-quench technique (Kaur et al., 2016). The melt-quench technique is the most widely used method for making glass composites because of its simplicity. This method generally has stages as shown in Fig. 1 (Muramoto et al., 2018). All precursors or raw materials are mixed into one container in the initial stage. In the second stage, a furnace melts the mixture at high temperatures. Some researchers use temperatures of 900 °C (Aly et al., 2020), 950 °C (Boonin et al., 2020), 1000 °C (Singh et al., 2021), 1100 °C (Mhareb et al., 2021), 1300 °C (Zakaly et al., 2021), and 1400 °C (M. H.A. Mhareb et al., 2020) The third stage, melted glass is poured into a mould to get a glass sample with the desired shape. In the last stage, the glass sample is removed or removed from the mould.

The parameters that are often used to assess the ability of glass composites as radiation shields are linear attenuation coefficient ($\mu$), mass attenuation coefficient ($\mu_m$), mean free path (MFP), tenth value layer (TVL), half value layer (HVL), atomic cross-section ($\sigma_{t,a}$), electronic cross-section ($\sigma_{t,el}$), effective electron density ($N_{eff}$), effective atomic number ($Z_{eff}$), and buildup factor (Ardiansyah et al., 2023; Khazaalah et al., 2022; M. M. Rafiei et al., 2020; Mustafa Mohammad Rafiei et al., 2020; Rafiei and Tavakoli-Anbaran, 2018). In several articles, experimentally, the radiation parameter values obtained were compared with theoretical values obtained from XCOM, Geant4, FLUKA, MCNP, and or Phy-X/PSD (Aşkin et al., 2020; Aşkın et al., 2019; Şakar et al., 2020). In addition, other properties such as physical, mechanical, and optical properties are also considered in several studies (Aladailah et al., 2022; Mahmoud et al., 2022; Singh et al., 2021). Physical properties were observed to determine the glass samples' tightness, rigidity, and structural change (Aboalatta et al., 2021).

As far as our investigation, no literature has been found that specifically discusses the use of BaO as a glass composite material made by a melt-quenching technique as a shield for gamma-ray radiation. Based on this, this paper presents data on the properties of glass-based radiation shielding materials containing BaO, such as physical, mechanical, optical, and radiation shielding properties obtained from several published literature in recent years.

## 2. Interaction of gamma rays with matter

Three possible interactions occur when gamma-ray photons from nuclear reactions interact with matter. The energy of the incoming photons strongly influences the interaction that occurs. If the incoming photon energy ranges from 0.01 MeV to 0.5 MeV, then the dominating interaction is the photoelectric effect. The dominant Compton effect occurs when the photon energy is $>$ 0.5 MeV. Then, pair production occurs at high energy ($\geq$ 1,02 MeV) (L'Annunziata, 2020; Murray and Holbert, 2015). The mechanism of the three interactions can be seen in Fig. 2.

### 2.1. Photoelectric effect

An illustration of the photoelectric effect can be seen in Fig. 2a. The photoelectric effect is a phenomenon that occurs when an atom completely absorbs incoming photon energy. All the absorbed photon energy is transferred to the electron in this state. When the incoming photon energy exceeds the electron's binding energy, the electron can be detached from the atom and produce ions. The energy of the emitted electron is equal to the energy of the incident photon minus the electron's binding energy. The released electrons (photoelectrons) can cause secondary ionization events as they move through the surrounding material (Kaur et al., 2016; L'Annunziata, 2020; Murray and Holbert, 2015).

### 2.2. Rayleigh scattering

Rayleigh scattering is a type of scattering interaction between low-energy photons and electrons tightly bound in atoms. This interaction, also called coherent or elastic scattering, occurs by temporarily

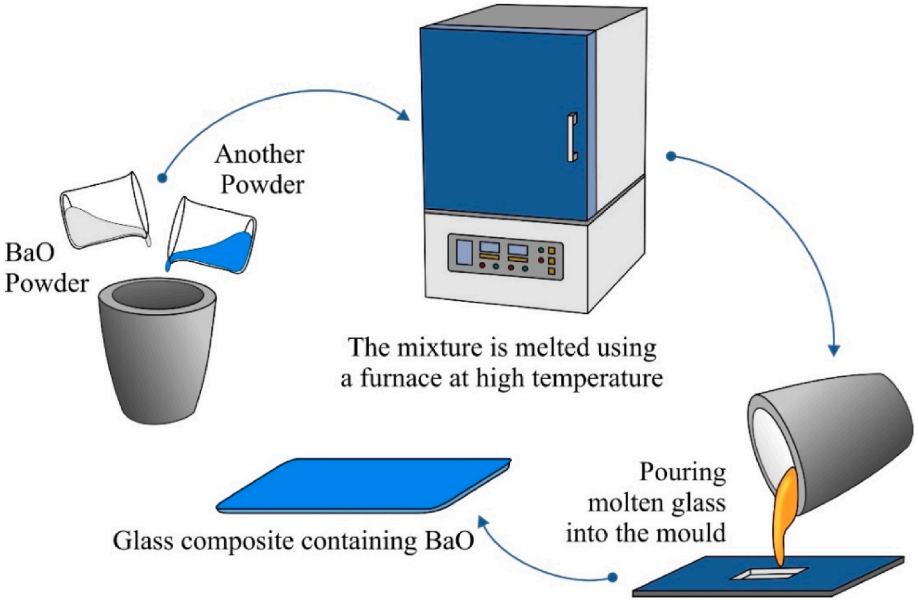


**Fig. 1.** Glass composite fabrication process using the melt-quench technique.

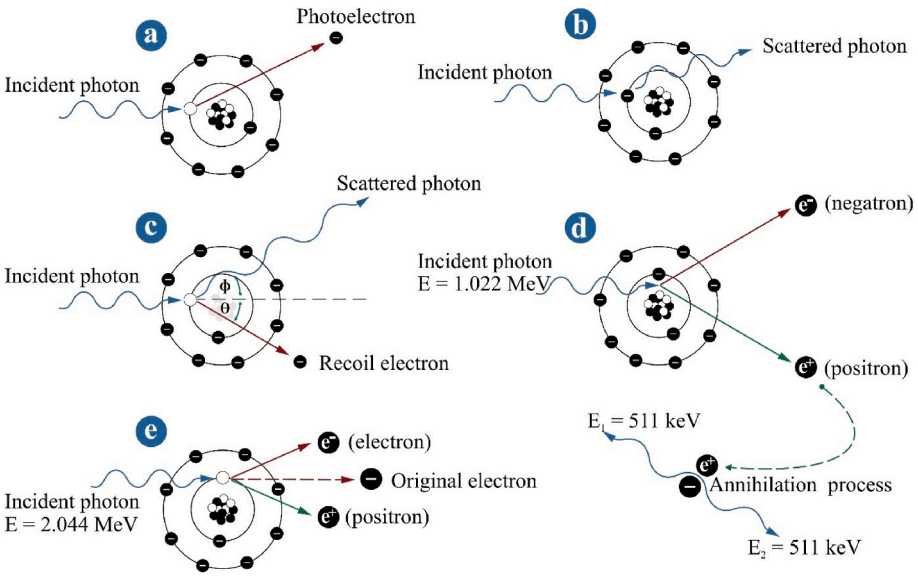


**Fig. 2.** Three mechanisms occur when photons interact with matter (a) Photoelectric effect, (b) Rayleigh scattering, (c) Compton scattering, (d) Electron–positron pair production, and (e) Pair production in the electron field.

increasing the energy of electrons without removing them from the atom. After that, the electron returns to its previous energy level by emitting a gamma ray photon of the same energy in a slightly different direction, as shown in Fig. 2b (Obodovskiy, 2019).

### 2.3. Compton scattering

An illustration of compton scattering can be seen in Fig. 2c. The Compton effect is a phenomenon in which an electron in an atom absorbs some of the photon's energy and then deflects it at an angle Φ. In contrast, the pounded electrons are thrown at an angle θ off the trajectory. The result of these interactions is the formation of ions. However, the deflected photon continues to travel through matter until all of its kinetic energy is exhausted by interacting with other electrons in the same way or through some other interaction mechanism (Kaur et al., 2016; L'Annunziata, 2020; Murray and Holbert, 2015).

### 2.4. Electron–positron pair production

Another mechanism that occurs when a photon hits a medium is the pair production illustrated in Fig. 2d. Pair production can occur when an incident photon has energy ≥ 1.022 MeV. When the photon approaches the atomic nucleus, the photon is destroyed and gives rise to two particles, namely negatron ($e^-$) and positron ($e^+$). When the positron collides with an electron, the particle is annihilated, giving rise to two new gamma rays with a total energy of 1.022 MeV. The two new photons emitted in opposite directions result from the law of conservation of momentum (Kaur et al., 2016; L'Annunziata, 2020; Murray and Holbert, 2015).

### 2.5. Pair production in the electron field

The interaction scheme between photons and matter in Fig. 2e is known as pair production in the electron field or triplet production. This interaction occurs when an incident photon has energy ≥ 2.044 MeV. Triplet production is a particular case of pair production that occurs near orbital electrons. Photons are annihilated, and their energy creates electrons and positrons. Orbital electrons also gain energy and are released from the atom (Chu et al., 2008; Hubbell, 2006).

## 3. Theoretical background

### 3.1. Physical properties

To determine some of the physical parameters of a material, basic information about it is density. The density of a glass composite can be determined by the Archimedes principle as shown in equation (1) (Aboud et al., 2022):

$$\rho = \frac{W_{air}}{W_{air} - W_{liquid}} \times \rho_{liquid} \tag{1}$$

where, $W_{air}$ and $W_{liquid}$ are the weight of the sample in air and liquid, respectively. Based on the value of density ($\rho$) and molar mass (M), the molar volume of a glass composite can be determined using equation (2). Molar volume ($V_m$) is the volume occupied by 1 mol of a chemical element or compound at standard temperature and pressure (STP). The $V_m$ is defined as the volume of the substance containing one mol% (Madshal et al., 2021).

$$V_m = \frac{M}{\rho} \tag{2}$$

The ion concentration (N), Polaron radius ($r_p$), inter-nuclear distance ($r_i$), and field strength ($F$) were computed also computed according to the following formulas, respectively (M H A Mhareb et al., 2020):

$$N = \frac{mole\% \times \rho \times N_A}{M_i} \tag{3}$$

$$r_p = \frac{1}{2}\left(\frac{\pi}{6N}\right)^{\frac{1}{3}} \tag{4}$$

$$r_i = \left(\frac{1}{N}\right)^{\frac{1}{3}} \tag{5}$$

$$F = \frac{Z}{r_p^2} \tag{6}$$

Where mole% is the mole fraction per cent, and Z is the mass number of barium. Ion concentration is a parameter used to determine the effect of alkaline metal cations on the properties of the host material. Polarons are quasiparticles that arise due to interactions between charge carriers and lattice ion vibrations, which are highly ionic or polar solid materials

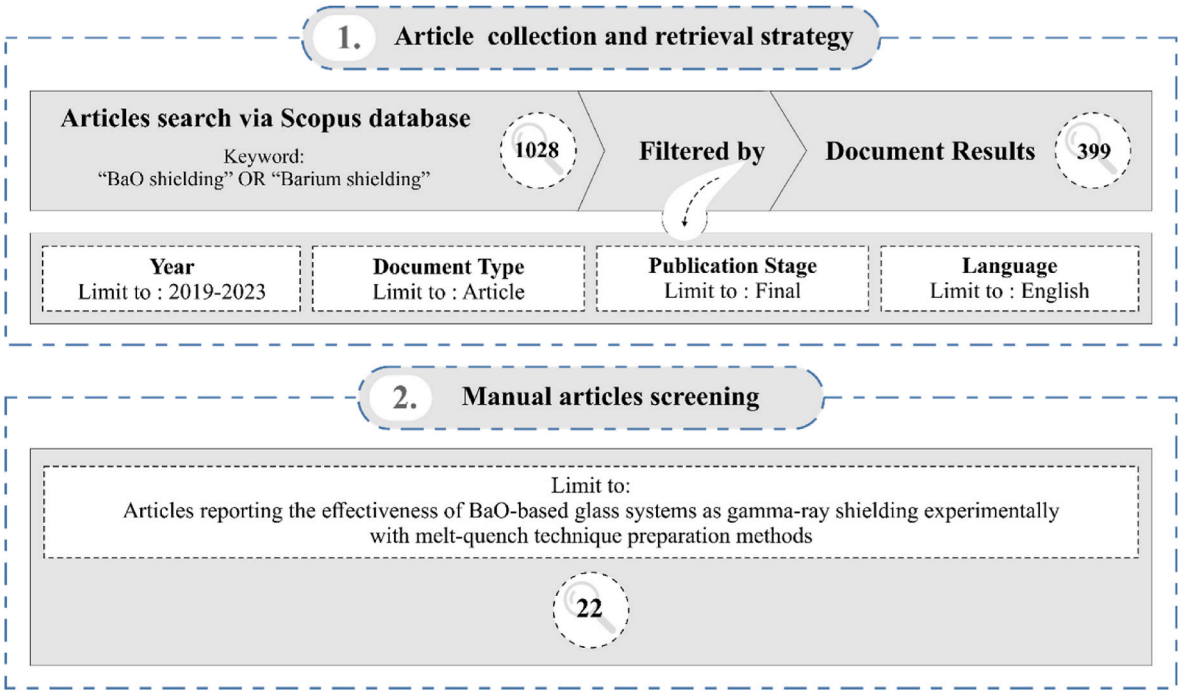


**Fig. 3.** The scheme of search strategy and data selection will be discussed in this article.

(Geidam et al., 2022). Polarons are pseudo particles that describe the interactions between electrons and ions and are also used to understand the interactions between electrons and atoms in solid materials (Madshal et al., 2021). The internuclear distance is the distance between two nuclei in a molecule.

On the other hand, there are some essential structural properties such as optical packing density (OPD), oxygen molar volume (*OMV*), packing density ($V_t$), and Poisson's ratio (σ). Oxygen packing density measures the compactness of glass structure by determining the packing of oxygen ions in a glass system. Oxygen molar volume represents the molar volume that contains one mol of oxygen atoms (Singh et al., 2021). Packing density was defined as the ratio between the minimum fraction of volume occupied by the ions and the corresponding effective volume of glass (Madshal et al., 2021). The packing density informs the atomic packing (Kaur et al., 2019). Poisson's ratio is defined as the ratio between lateral and longitudinal strain produced when tensile force is applied (Saddeek et al., 2018). These parameters were deduced from molar volume values and calculated using the following equations (M H A Mhareb et al., 2020):

$$OPD = \left(\frac{\rho}{M}\right) \times n \times 1000 \tag{7}$$

$$OMV = \frac{V_m}{\sum_i x_i n_i} \tag{8}$$

$$V_t = \sum_i \frac{V_i x_i}{V_m} \tag{9}$$

$$\sigma = 0.5 - \left(\frac{1}{7.2 V_t}\right) \tag{10}$$

Where $n$, $n_i$, $x_i$ $V_i$ denote the total number of oxygen atoms, the fraction of oxygen atoms, the mole fraction of the oxides, and packing factor, respectively. Packing factor obtained for respective oxide constituent $A_XO_Y$ as (Aladailah et al., 2022):

$$V_i = 6.032 \times 10^{23} \times \frac{4}{3}\pi\left(XR_A^3 + YR_O^3\right) \tag{11}$$

$R_A$ and $R_O$ are the ionic radii of metal A and oxygen O, respectively.

### 3.2. Mechanical properties

Mechanical properties must be known to understand a glass material's stiffness, strength, and hardness (Singh et al., 2021). The elastic constants are very interesting in solid structures because they are directly related to the interatomic forces and potentials (El-Mallawany et al., 1994). One of the theoretical models that can provide information about the mechanical properties of materials is the Makishima-Mackenzie model. This model considers the value of packing density ($V_t$), oxide dissociation energy ($G_i$), and mole fraction of the i-th oxide component ($X_i$) to calculate the value of the young's modulus ($Y$) of the glass system (Mahmoud et al., 2022):

$$Y = 83.6\, V_t \sum_i G_i X_i \tag{12}$$

When $G_i$ is entered in kcal/cm$^3$ units, and the $Y$ value is in kbar units. Other elastic modulus values such as bulk modulus ($K$), shear modulus ($S$), and longitudinal modulus ($L$) in GPa units can be calculated using equation 13–15 (El-Moneim et al., 2022; Singh et al., 2021):

$$K = 10.0\, V_t^2 G_t \tag{13}$$

$$S = \frac{3K}{(10.2\, V_t - 1)} \tag{14}$$

$$L = K + \frac{4S}{3} \tag{15}$$

The total dissociation energy ($G_t$) in units of kcal/cm$^3$ in equation (13) can be calculated using equation (16) (Singh et al., 2021):

$$G_t = \sum_i G_i X_i \tag{16}$$

In addition to the elastic modulus, the Makishima-Mackenzie model also offers an equation that can be used to determine the hardness ($H$) of a glass sample by considering the Poisson ratio ($\sigma$) and Young's modulus ($Y$) as in equation (17) (Singh et al., 2021).

**Table 1**
The chemical composition of several barium-based glass oxides that will be discussed in this article (alloys of metals and metalloids).

| Ref. | Barium based glass compositions (in weight percentage) | | | | | | | | | | | | | | | | | | Sample Code |
|---|---|---|---|---|---|---|---|---|---|---|---|---|---|---|---|---|---|---|---|
| | $Bi_2O_3$ | BaO | $B_2O_3$ | PbO | $SiO_2$ | NaO | $Al_2O_3$ | $TiO_2$ | ZnO | $TeO_2$ | $Na_2O$ | CaO | $Dy_2O_3$ | SrO | $MoO_3$ | CdO | $V_2O_5$ | SLS | |
| Kaur et al. (2019) | 65 | 10 | 25 | - | - | - | - | - | - | - | - | - | - | - | - | - | - | - | SC01 |
| Almatari et al. (2019) | - | 5 | 50 | 45 | - | - | - | - | - | - | - | - | - | - | - | - | - | - | SC02 |
| Aly et al. (2020) | - | 60 | 10 | - | 20 | 5 | 5 | - | - | - | - | - | - | - | - | - | - | - | SC03 |
| Aşkin et al. (2020) | - | 10 | 50 | 40 | - | - | - | - | - | - | - | - | - | - | - | - | - | - | SC04 |
| (M. H.A. Mhareb et al., 2020) | - | 30 | 50 | - | 10 | - | - | 10 | - | - | - | - | - | - | - | - | - | - | SC05 |
| Boonin et al. (2020) | - | 25 | - | - | - | - | - | - | 10 | 65 | - | 10 | - | - | - | - | - | - | SC06 |
| Zakaly et al. (2021) | - | 30 | 20 | - | 15 | - | 5 | - | - | - | 20 | 10 | - | - | - | - | - | - | SC07 |
| Aboalatta et al. (2021) | - | 50 | 25 | - | - | - | - | - | 10 | - | 10 | - | 5 | - | - | - | - | - | SC08 |
| Tashlykov et al. (2021) | 5 | 35 | 60 | - | - | - | - | - | - | - | - | - | - | - | - | - | - | - | SC09 |
| (D'Souza et al., 2021) | 10 | 8 | 50 | - | 20 | - | - | - | 12 | - | - | - | - | - | - | - | - | - | SC10 |
| Dwaikat et al. (2021) | - | 20 | 25 | - | - | - | - | - | - | 30 | - | - | - | 10 | 15 | - | - | - | SC11 |
| Khazaalah et al. (2022) | 19.2 | 4 | 19.2 | - | - | - | - | - | 28.8 | - | - | - | - | - | - | - | - | 28.8 | SC12 |
| Singh et al. (2022) | - | 30 | 50 | - | - | - | 10 | - | - | - | 10 | - | - | - | - | - | - | - | SC13 |
| Aboud et al. (2022) | 10 | 10 | 50 | 20 | - | - | - | - | - | - | - | - | - | - | - | 10 | - | - | SC14 |
| Fidan et al. (2022) | - | 5 | 35 | - | - | - | - | - | - | 34 | - | - | - | - | - | - | 1 | - | SC15 |
| Chinthakayala et al. (2022) | 45 | 45 | 10 | - | - | - | - | - | - | - | - | - | - | - | - | - | - | - | SC16 |
| Mahmoud et al. (2022) | - | 40 | 60 | - | - | - | - | - | - | - | - | - | - | - | - | - | - | - | SC17 |
| Mhareb et al. (2022) | - | 20 | 35 | - | - | - | - | - | - | 35 | - | - | - | 10 | - | - | - | - | SC18 |
| Aladailah et al. (2022) | - | 40 | - | - | 45 | - | - | - | - | - | - | 15 | - | - | - | - | - | - | SC19 |
| Imheidat et al. (2022) | - | 20 | - | - | - | - | - | - | - | 50 | - | - | - | 10 | 20 | - | - | - | SC20 |

$$H = \frac{(1-2\sigma)Y}{6(1+\sigma)} \tag{17}$$

### 3.3. Optical properties

The basic information that needs to be known to determine the optical properties of a glass system is the energy gap ($E_g$). By using the Mott and Davis equation (equation (18)), the value of $E_g$ can be calculated (Mahmoud et al., 2022):

$$h\nu\alpha = A\left(h\nu - E_g\right)^n \tag{18}$$

Where $h$, $\nu$, $\alpha$, and $A$ are plank constants, photon frequencies, absorption coefficients and constants, respectively. Based on the $E_g$ value, the refractive index ($n$) can be determined using equation (19) (M. H.A. Mhareb et al., 2020):

$$\frac{(n^2-1)}{(n^2+2)} = 1 - \sqrt{\frac{E_g}{20}} \tag{19}$$

Using the values of refractive index ($n$), Dielectric constant ($\varepsilon$), optical dielectric constant ($\varepsilon^{'}$), Reflection loss ($R_L$), and transmission ($T$) can be determined using equations (20) and (23) (Dwaikat et al., 2021):

$$\varepsilon = n^2 \tag{20}$$

$$\varepsilon^{'} = n^2 - 1 \tag{21}$$

$$R_L = \frac{(n^2-1)}{(n^2+2)} \tag{22}$$

$$T = \frac{2n}{n^2+1} \tag{23}$$

Then, taking into account the value of the refractive index ($n$) and the molar volume ($V_m$), the molar refractivity ($R_m$) can be calculated by equation (24). Molar refractivity informs about the total polarizability of a mole (Kaur et al., 2019).

$$R_m = V_m\frac{(n^2-1)}{(n^2+2)} \tag{24}$$

Two other quantities that can be calculated using the value of molar refractivity ($R_m$) are molar polarizability ($\alpha_m$) and metallization criteria ($M$). The equation for calculating these two quantities is shown in equations (25) and (26):

$$\alpha_m = \left(\frac{3}{4\pi N_A}\right)R_m \tag{25}$$

$$M = 1 - \left(\frac{R_M}{V_M}\right) \tag{26}$$

In addition to the refractive index ($n$), optical electronegativity ($\chi$) can be determined based on the value of the band gap ($E_g$). Optical electronegativity measures the attraction of electrons from the oxide ion attached to the ion. If the electronegativity is high, the ion strongly attracts electrons from the bound oxide ions, keeping the ions tightly bound in the network (Kaur et al., 2019). The relationship between $\chi$ and $E_g$ is contained in equation (27):

$$\chi = 0.2688 \times E_g \tag{27}$$

Based on the $\chi$ value, electron polarizability ($a_0$) and optical basicity ($\Lambda$) can be calculated using equations (28) and (29):

$$a_0 = -0.9\chi + 3.5 \tag{28}$$

$$\Lambda = -0.5\chi + 1.7 \tag{29}$$

**Table 2**
The chemical composition of several barium-based glass oxides that will be discussed in this article (alloys of metals, metalloids, and non-metals).

| Ref. | Barium based glass compositions (in weight percentage) | | | | | | | Sample Code |
|---|---|---|---|---|---|---|---|---|
| | BaO | $SiO_2$ | ZnO | $Na_2O$ | $H_3BO_3$ | $K_2O$ | $P_2O_5$ | |
| Mhareb et al. (2021) | 30 | - | 10 | 10 | 50 | - | - | SC21 |
| Singh et al. (2021) | 10 | 20 | - | 7.5 | - | 7.5 | 55 | SC22 |

**Table 3**
Physical properties of several glass systems.

| Properties | Sample code | | | | | | | | | | | |
|---|---|---|---|---|---|---|---|---|---|---|---|---|
| | SC01 | SC05 | SC06 | SC08 | SC09 | SC12 | SC13 | SC15 | SC17 | SC18 | SC20 | SC22 |
| Molar volume ($V_m$) ($cm^3$/mol) | 35.886 | 25.229 | 28.143 | 28.210 | 25.845 | 28.520 | 30.503 | 26.210 | 28.287 | 25.067 | - | 41.596 |
| Ion concentration (N) × $10^{23}$ (ion/$cm^3$) | - | 7.16 | - | 1.067 | - | - | 5.921 | - | - | 4.804 | - | 0.005 |
| Polaron radius ($r_p$) × $10^{-9}$ | - | 4.505 | - | 8.497 | - | - | 4.799 | - | - | 5.146 | - | 23.464 |
| Inter-nuclear distance ($r_p$) × $10^{-8}$ | - | 1.1178 | - | 2.1083 | - | - | 1.1908 | - | - | 1.2767 | - | 5.8217 |
| Field strength (F) × $10^{18}$ | - | 6.770 | - | 3.601 | - | 0.031 | 8.364 | - | - | 5.189 | - | - |
| Oxygen packing density (OPD) (g.atom/l) | 77.151 | 87.200 | 109.34 | 56.717 | - | 72.09 | 72.124 | - | - | 81.7812 | - | 81.738 |
| Oxygen molar volume (OMV) ($cm^3$/mol) | 12.962 | 11.467 | - | 17.631 | - | - | 13.865 | - | - | 12.2277 | - | - |
| Packing density ($V_t$) | 0.594 | 0.695 | - | 0.525 | 0.683 | - | - | - | - | 0.6513 | 1.02 | 0.61 |
| Poisson's ratio ($\sigma$) | 0.266 | 0.403 | - | 0.236 | 0.297 | - | 0.259 | 0.25 | 0.282 | - | 0.364 | 0.27 |

**Table 4**
Mechanical properties of various glazing systems.

| Properties | Sample code | | | | |
|---|---|---|---|---|---|
| | SC09 | SC15 | SC17 | SC20 | SC22 |
| Young's modulus (Y) (GPa) | 99.73 | 134.97 | - | 111 | 68.61 |
| Bulk modulus (B) (GPa) | 81.75 | 89.98 | - | 136 | 50.31 |
| Shear modulus (S) (GPa) | 38.45 | 53.99 | - | 40.7 | 28.73 |
| Longitudinal modulus (L) (GPa) | 133.02 | 161.96 | - | 167 | 88.62 |
| Hardness (H) (GPa) | 5.21 | 8.998 | 5.252 | 3.68915 | 4.07 |

### 3.4. Gamma radiation shielding properties

The quantities that need to be determined to determine the effectiveness of a material in absorbing radiation are: total linear attenuation coefficient ($\mu$), total mass attenuation coefficient ($\mu_m$), atomic cross-section ($\sigma_{t,a}$), electronic cross-section ($\sigma_{t,el}$), half-value layer (HVL), tenth value layer (TVL), mean free path (MFP), effective atomic number ($Z_{eff}$), and electron density ($N_{eff}$) (Ardiansyah et al., 2022; Kaur et al., 2016). The total linear attenuation coefficient describes the fraction of the absorber absorbed or scattered gamma rays per unit thickness. This value represents the number of atoms in a volume of material and the possibility of photons being scattered or absorbed by the nucleus or electrons of one of the atoms (Singh et al., 2015; Singh and Badiger, 2013). Based on Lambert's Law, the total linear attenuation coefficient can be calculated through the following equation:

$$I = I_0 e^{-\mu x} \tag{30}$$

where $I$ and $I_0$ respectively indicate the intensity of the photons after and before passing through the glass sample, then x is the thickness of the sample in cm units. Based on the value of the total linear attenuation coefficient and density ($\rho$), the value of the total mass attenuation coefficient can be determined using equation (31). The total mass attenuation coefficient is a parameter that describes the fraction of photons removed by a glass sample per unit mass (B. Hiremath et al., 2023).

$$\mu_m = \frac{\mu}{\rho} = \frac{ln(I_0/I)}{\rho x} \tag{31}$$

Other units that can be determined based on the $\mu$ value are HVL, TVL, and MFP. HVL is the thickness of the interacting materials at which the intensity of the photon beam entering it is reduced by half. TVL describes the absorber thickness that attenuates the intensity of an incident photon beam by 90%. MFP is the average distance photons can travel in a matter before interacting (Singh et al., 2021)(Ardiansyah et al., 2023). These three quantities can be calculated based on the following equation:

$$HVL = \frac{ln\ 2}{\mu} \approx \frac{0.693}{\mu} \tag{32}$$

$$TVL = \frac{ln\ 10}{\mu} \approx \frac{2.303}{\mu} \tag{33}$$

**Table 5**
Optical properties of various glass systems.

| Properties | Sample code | | | | | | |
|---|---|---|---|---|---|---|---|
| | SC01 | SC05 | SC06 | SC07 | SC11 | SC18 | SC20 |
| Energy gap ($E_g$) (eV) | 2.6200 | 3.3580 | 2.9120 | 3.3300 | 3.0010 | 3.4586 | 3.1084 |
| Refractive index (n) | 2.5100 | 2.3060 | 1.8620 | 2.3135 | 2.3960 | 2.2834 | 2.3684 |
| Optical electronegativity ($\chi$) | 0.7043 | 0.9026 | 0.7827 | 0.8951 | 0.8060 | 0.9296 | 0.8355 |
| Dielectric constant ($\varepsilon$) | 6.3001 | 5.3210 | 3.4670 | 5.3521 | 5.7440 | 5.2141 | 5.6097 |
| Optical dielectric constant ($\varepsilon'$) | 5.3001 | 4.3210 | 2.4670 | 4.3521 | 4.7440 | 4.2141 | 4.6097 |
| Molar refractivity ($R_m$) ($cm^{-3}$) | 22.90 | 14.8910 | 12.6700 | - | 15.7430 | 14.6428 | 15.9921 |
| Reflection loss ($R_L$) | 0.6386 | 0.5900 | 0.4513 | 0.5920 | 0.6120 | 0.5841 | 0.6057 |
| Metallization criteria (M) | 0.3619 | 0.4090 | 0.5480 | - | 0.3870 | 0.4158 | 0.3942 |
| Electron polarizability ($\alpha_0$) | 2.8700 | 2.6870 | 2.7955 | 2.6944 | 2.7730 | 2.6632 | 2.7480 |
| Optical basicity ($\Lambda$) | 1.2480 | 1.2480 | 0.8970 | 1.2524 | 1.2960 | 1.2351 | 1.2822 |
| Molar polarizability ($\alpha_0$) × $10^{-24}$ | 9.0745 | 5.6610 | 5.0310 | - | 6.2440 | 5.8078 | 6.3430 |
| Transmission (T) | 0.6877 | 0.7290 | 0.8337 | 0.7284 | 0.7100 | 0.7349 | 0.7166 |

**Table 6**
Density and radiation shielding properties of several glass systems obtained experimentally at 0.662 MeV.

| Sample code | Properties | | | | | |
|---|---|---|---|---|---|---|
| | $\rho$ (g/cm$^3$) | $\mu$ (cm$^{-1}$) | $\mu_m$ (cm$^2$/g) | HVL (cm) | TVL (cm) | MFP (cm) |
| SC01 | 4.942 | 0.4814 | 0.0974 | 1.4400 | 4.7836 | 2.0775 |
| SC02 | 5.454 ± 0.055 | 0.4875 | 0.0894 | 1.4219 | 4.7235 | 2.0514 |
| SC03 | 3.8903 ± 0.001 | 0.3120 | 0.0802 | 2.2216 | 7.3801 | 3.2051 |
| SC04 | 5.312 | 0.4664 | 0.0878 | 1.4862 | 4.9370 | 2.1441 |
| SC05 | 3.758 ± 0.002 | 0.2879 | 0.0766 | 2.4079 | 7.9989 | 3.4739 |
| SC06 | 5.3462 ± 0.0002 | 0.4040 | 0.0756 | 1.7156 | 5.6991 | 2.4751 |
| SC07 | 3.652 | 0.2735 | 0.0749 | 2.5340 | 8.4179 | 3.6558 |
| SC08 | 4.020 ± 0.008 | 0.3094 | 0.0770 | 2.2406 | 7.4430 | 3.2325 |
| SC09 | 3.281 | 0.2840 | 0.0866 | 2.4370 | 8.1077 | 3.5211 |
| SC10 | 4.140 | 0.4426 | 0.1069 | 1.5662 | 5.2028 | 2.2595 |
| SC11 | 4.977 | 0.3890 | 0.0782 | 1.7819 | 5.9192 | 2.5707 |
| SC12 | 5.249 | 0.3244 | 0.0618 | 2.1378 | 7.0982 | 3.0848 |
| SC13 | 3.187 | 0.2425 | 0.0761 | 2.8424 | 9.4940 | 4.1232 |
| SC14 | 3.975 | 0.3685 | 0.0927 | 1.8810 | 6.2485 | 2.7137 |
| SC15 | 5.490 | 0.5051 | 0.0920 | 1.3724 | 4.5589 | 1.9799 |
| SC16 | 7.145 | 0.7216 | 0.1010 | 0.9370 | 3.1160 | 1.3857 |
| SC17 | 3.148 ± 0.062 | 0.2644 | 0.0840 | 2.6213 | 8.7077 | 3.7817 |
| SC18 | 4.7395 | 0.3782 | 0.0798 | 1.8327 | 6.0881 | 2.6440 |
| SC19 | 3.513 ± 0.014 | 0.2740 | 0.0780 | 2.5296 | 8.4032 | 3.6494 |
| SC20 | 5.667 | 0.4001 | 0.0706 | 1.7325 | 5.7552 | 2.4994 |
| SC21 | 3.754 | 0.2842 | 0.0757 | 2.4391 | 8.1026 | 3.5189 |
| SC22 | 2.816 | 0.2157 | 0.0766 | 3.2160 | 10.6747 | 4.6359 |

$$MFP = \frac{1}{\mu} \tag{34}$$

By using $\mu_m$, the values of total atomic cross-sections ($\sigma_{t,a}$) and electronic cross-sections ($\sigma_{t,el}$) can be determined based on equations (35) and (36). The total atomic cross-sections are the most likely individual processes by which photons interact with atoms (Abd-Allah et al., 2019).

$$\sigma_{t,a} = \frac{\mu_m}{N_A \sum_i^n (w_i/A_i)} \tag{35}$$

$$\sigma_{t,el} = \frac{1}{N_A} \sum_i^n \frac{f_i A_i}{Z_i} (\mu_m)_i \tag{36}$$

Based on $\sigma_{t,a}$ and $\sigma_{t,el}$, the effective atomic number ($Z_{eff}$) can be determined using the following equation:

$$Z_{eff} = \frac{\sigma_{t,a}}{\sigma_{t,el}} \tag{37}$$

$Z_{eff}$ is a number that represents the number of atoms in materials, alloys, or compounds, and this value varies depending on the photon energy introduced by Hine in 1952. In addition, the radiation parameter can be calculated by considering $\mu_m$ and $\sigma_{t,el}$, that is the effective electron density ($N_{eff}$). Effective electron density refers to the number of electrons per unit mass of a substance that interacts, and the likelihood of photon interaction increases when the electron density increases (Levet and Özdemir, 2017). Electron density is the number of electrons per mass which indicates that the higher the value, the greater the possibility of photon interactions and can be calculated by the following formula (Boonin et al., 2020):

$$N_{el} = \frac{\mu_m}{\sigma_{t,el}} \tag{38}$$

Another radiation parameter that is very important to know is the Buildup factor. The value of this parameter indicates the possible dispersion of a photon (Sabry et al., 2022). Buildup factors such as exposure buildup factors (EBFs) and energy absorption buildup factors (EABFs) could be estimated (El-Mallawany et al., 2020). The two parameters we have to measure before buildup factors are $R$ and $Z_{eq}$, shown in equations (39) and (40), respectively (El-Mallawany et al., 2020).

$$R = \frac{(\mu/\rho)_{Compton}}{(\mu/\rho)_{Total}} \tag{39}$$

$$Z_{eq} = \frac{Z_1(log\ R_2 - log\ R) + (log\ R - log\ R_1)}{log\ R_2 - log\ R_1} \tag{40}$$

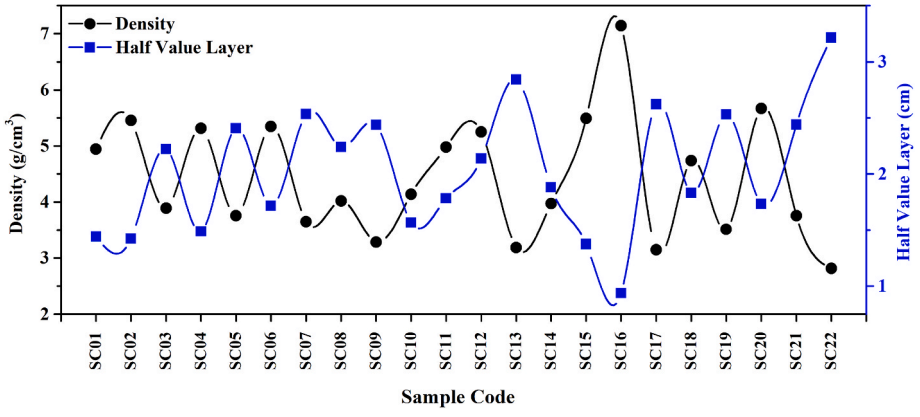


**Fig. 4.** Comparison of density and HVL obtained experimentally at 0.662 MeV.

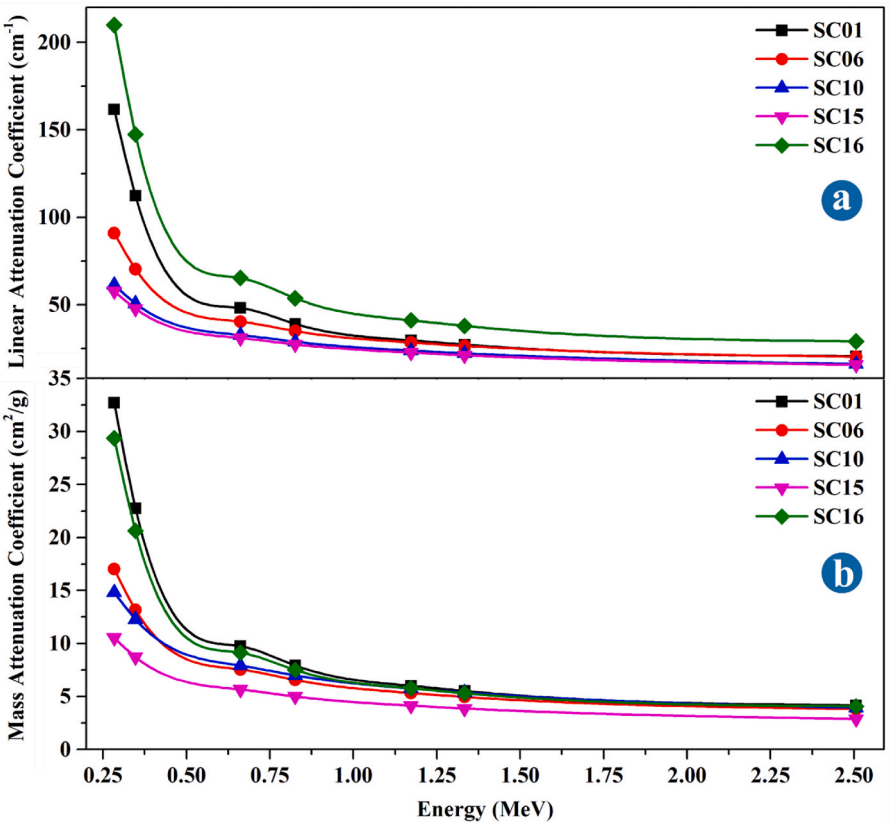


**Fig. 5.** (a) Linear attenuation coefficient ($\mu$), and (b) Mass attenuation coefficient ($\mu_m$) obtained via Phy-X/PSD software from five glass samples reporting the highest HVL experimentally.

where $Z_1$ and $Z_2$ are the atomic numbers related to the ratios $R_1$ and $R_2$, respectively. Then, the $Z_{eq}$ is a virtual atomic number that describes the atomic number of the complex material when photons are scattered, and the $Z_{eq}$ can be used to compute the GP-parameters through equation (41) (Sabry et al., 2022):

$$P = \frac{P_1(\log Z_2 - \log Z_{eq}) + P_2(\log Z_{eq} - \log Z_1)}{\log Z_2 - \log Z_1} \tag{41}$$

where $P_1$ and $P_2$ refer to the values of GP-fitting parameters corresponding to $Z_1$ and $Z_2$ at a certain energy, respectively. P is the GP-fitting parameters calculated via the Phy-X/PSD program. Then, using the P parameter, the EBF or/and EABF values can be calculated using equations (42) and (43) according to the conditions (El-Mallawany et al., 2020):

$$B(E,X) = 1 + \frac{b-1}{K-1}(K^x - 1), \rightarrow \text{for } K \neq 1 \tag{42}$$

$$B(E,X) = 1 + (b-1)x, \rightarrow \text{for } K = 1 \tag{43}$$

E and X represent the primary photon energy (X = 0.5 to 40 mfp) and penetration depth (P.D.), respectively. In addition, the function K (E, X) can be evaluated by equation (44):

$$K(E,X) = Cx^a + d\frac{tanh\left(\frac{x}{X_k} - 2\right) - tanh(-2)}{1 - tanh(-2)}, \rightarrow \text{for } x \leq 40\ mfp \tag{44}$$

Here, the combination of K(E, X) and X performs a multiplicative factor on the photon dose to assess the spectrum's shape.

## 4. Data collection

The literature analyzed for this article's physical, mechanical, optical and radiation shielding properties was collected from Scopus by entering the keywords "BaO Shielding" or "Barium Shielding". A total of 1028 articles containing these keywords in the title, abstract, and keywords section are displayed. Furthermore, the search is limited to documents in the form of English articles published in the last 5 years, namely from 2019 to 2023. After these restrictions, the literature displayed remains 399 documents. The document is then exported as a comma-separated values (csv) file. The next step is to read the title, abstract, and contents of the articles that have been exported to find articles that report the effectiveness of BaO-based glass systems experimentally as shielding. Then, in line with our description in the introductory part of this article, we chose literature that uses the melt-quench technique method. Finally, the remaining 22 articles were selected to be discussed in this study. The scheme for selecting articles whose data will be used in this study can be seen in Fig. 3. The best data reported from each article are tabulated in Tables 1 and 2 accompanied by a sample code which will later be used for subsequent discussions.

## 5. Discussion

### 5.1. Physical properties

Physical properties are essential properties to be studied to clarify any changes in the structure of glass materials (M. H.A. Mhareb et al., 2020). Among the 22 glass material compositions in Tables 1 and 2, there were 12 samples whose physical properties were reported: SC01, SC05, SC06, SC08, SC09, SC12, SC13, SC15, SC17, SC18, SC20, and SC22. The physical properties of such glass samples are reported in articles such as molar volume ($V_m$), ion concentration (N), polaron radius

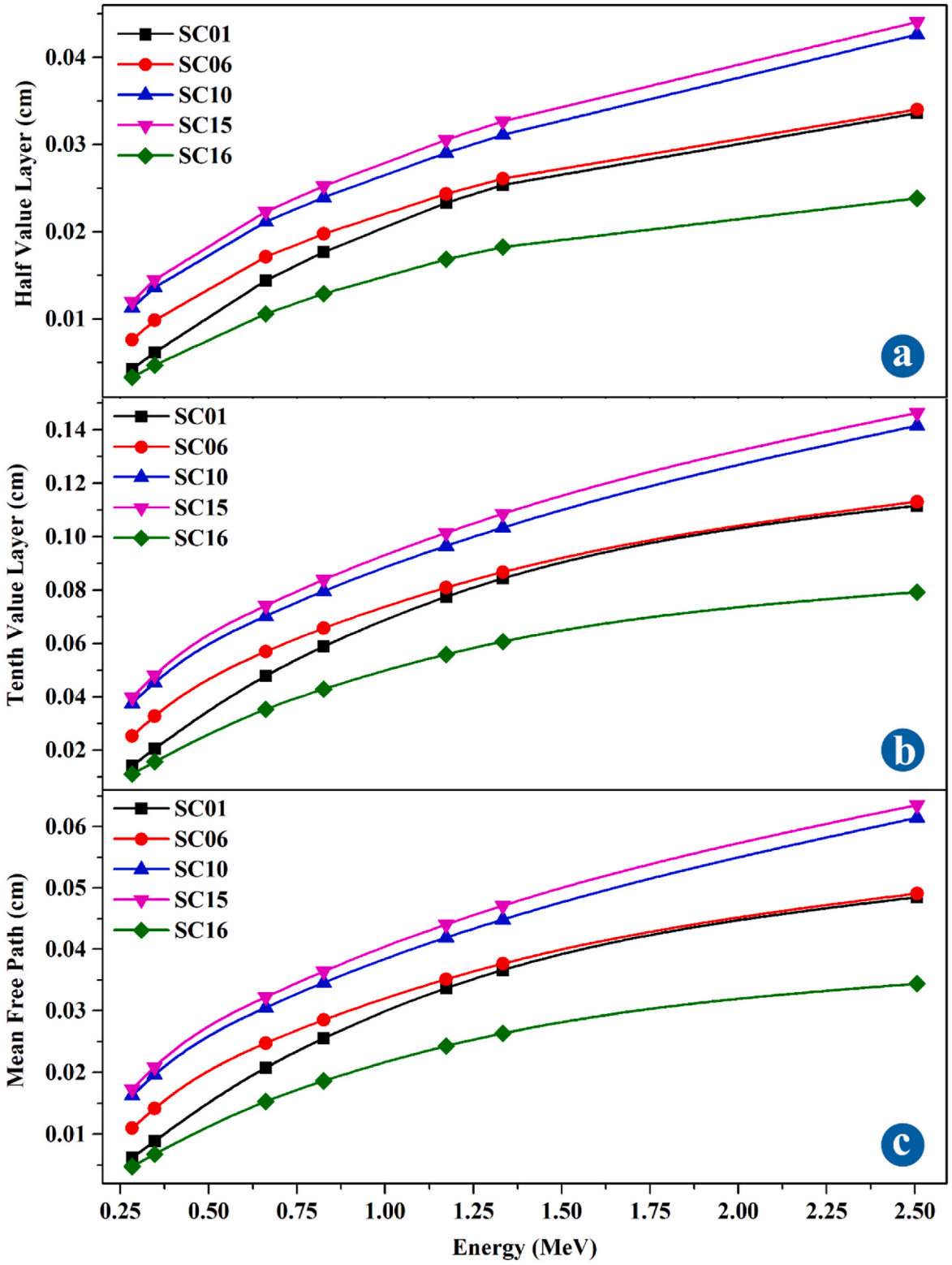


**Fig. 6.** (a) Mean free path (MFP), (b) Tenth value layer (TVL), and (c) Half value Layer (HVL) obtained via Phy-X/PSD software from five glass samples reporting the highest HVL experimentally.

($r_p$), inter-nuclear distance ($r_i$), field strength (F), oxygen packing density (OPD), oxygen molar volume (OMV), packing density ($V_t$), and poisson's ratio ($\sigma$) ditabulasikan pada Table 3. As confirmed from Tables 1 and it can be seen that samples SC01 and SC09 are $Bi_2O_3$–BaO–$B_2O_3$ glass systems, both of which differ only in the composition of the mixture where SC09 has a higher amount of BaO than SC01. Based on the article (Kaur et al., 2019), where the composition of BaO and $Bi_2O_3$ is varied ($Bi_2O_3$ remains), it is reported that increasing BaO can reduce packing density. The packing density informs about packing atoms and decreasing packing density impacts the expansion of the glass system (Kaur et al., 2019; M. H.A. Mhareb et al., 2020). If only based on the amount of BaO, the packing density of SC09 should be lower than

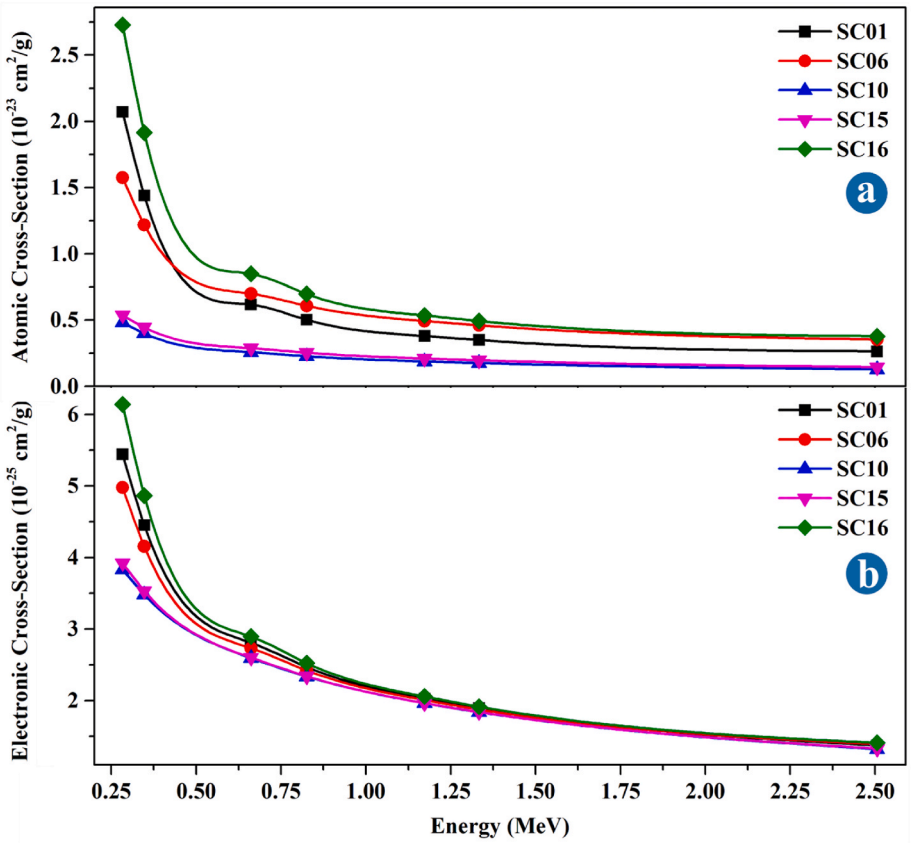


**Fig. 7.** (a) Atomic Cross-Section ($\sigma_{t,a}$) and (b) Electronic Cross-Section ($\sigma_{t,el}$) obtained via Phy-X/PSD software from five glass samples reporting the highest HVL experimentally.

SC01. However, based on Table 3, the packing density of SC09 is greater than SC01 where SC09 and SC01 are 0.683 and 0.594, respectively. This led to speculation that in the $Bi_2O_3$–BaO–$B_2O_3$ glass system, $Bi_2O_3$ has a significant effect. This statement is in line with the results of the research reported by (Kaewkhao et al., 2008) on the glass system $x$ $Bi_2O_3$:(60-$x$) BaO:40$B_2O_3$ with $10 \leq x \leq 50$ (in mol%). Density and molar volume studies have shown that $Bi_2O_3$ functions partly as a network modifier and partly as a network former in these glasses. Then in 2022, Mahmoud et al. reported that the molar volume of the 40BaO–60$B_2O_3$ (SC17) glass system was higher than that of 5$Bi_2O_3$–35BaO–60$B_2O_3$ (SC09), which also contradicts the statement presented by Kaur et al., in 2019. These results further strengthen the previous statement. To get a BaO-based glass system that has a high packing density, it can be done by adding $SiO_2$ and $TiO_2$ as in the sample coded SC05. The BaO–$B_2O_3$–$SiO_2$–$TiO_2$ glass system on SC05 has a higher packing density value than the $Bi_2O_3$–BaO–$B_2O_3$ glass system (SC01 and SC09), even the largest among other glass systems in Table 3.

### 5.2. Mechanical properties

There are 5 out of 22 BaO-based glass system sample codes whose mechanical properties have been reported in reference articles, namely SC09, SC15, SC17, SC20, and SC22. The mechanical properties of the five samples can be seen in Table 4. SC15 is the sample that has the highest young's modulus ($Y$), shear modulus ($S$), and hardness ($H$), while SC20 is the sample with the highest bulk modulus and longitudinal modulus. The value of the elastic coefficient of the glass system containing tellurite with the addition of barium oxide like SC15 is about three times greater than that of the tellurite-based glass system without barium, as reported by (El-Mallawany et al., 1994). Based on the report of Mhareb et al., in 2021 observing the effect of BaO on the mechanical properties of $SiO_2$–$Na_2O$–$K_2O$–$P_2O_5$–BaO (SC21) glass systems, a large amount of BaO will cause the elastic modulus value of glass to decrease. This decrease indicates that the glass structure has become stiffer and less impact-resistant. One reason for the decrease in the elastic modulus with increasing BaO may be because barium oxide (BaO) dissociation energy is low. The statement regarding the decrease in the elastic modulus of the glass system due to dissociation energy is supported by the results of Imheidat et al., in 2022. According to a report by Imheidat et al., in 2022, decreasing the content of $TeO_2$ and increasing $MoO_3$ in the $MoO_3$–$TeO_2$–BaO–SrO (SC20) glass system, can increase the dissociation energy per unit volume which is in line with the increase in the elastic modulus of the glass system. However, the statement regarding a decrease in the elastic modulus of glass due to an increase in BaO is not in line with the results of a study reported by Fidan et al., (2022). According to Fidan et al. in their article published in 2022, increasing the BaO content in the $B_2O_3$–$TeO_2$–BaO–PbO–$V_2O_5$ (SC15) glass system was able to increase its elastic modulus. The increase in the elastic modulus of the glass is attributed to its hardness and high connectivity due to the increase in the number of lattice bonds per unit volume of glass and the average cross-link density in the glass (Fidan et al., 2022) Based on these statements and the composition of the glass system in Tables 1 and 2, it is speculated that the elastic modulus may very well depend on the addition of non-metallic elements to the glass system.

### 5.3. Optical properties

The list of sample codes in Table 1, whose optical properties are reported in the original article, is tabulated in Table 5. From the table, it can be seen that the $E_g$ values range from 2.62 to 3.46 eV SC01 is the sample with the smallest $E_g$ obtained from the $Bi_2O_3$–BaO–$B_2O_3$ glass system, namely 2.62 MeV. According to the reference article containing

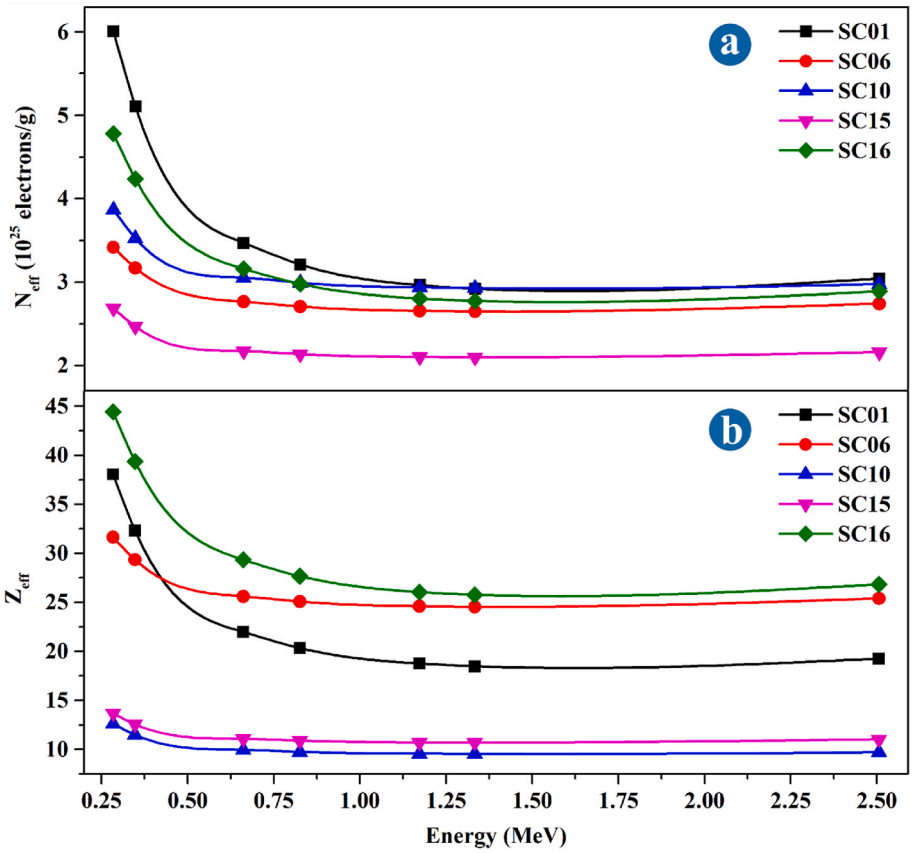


**Fig. 8.** (a) Effective electron density ($N_{eff}$) and (b) Effective atomic number ($Z_{eff}$) obtained via Phy-X/PSD software from five glass samples that reported the highest HVL experimentally.

sample SC01, the $E_g$ in the glass, system can continue to decrease as the BaO composition is added. The decrease in the $E_g$ is in line with the decrease in the value of optical electronegativity but increases the value of refractive index, molar refractivity, electron polarization, optical electronegativity, and optical basicity (Abd-Allah et al., 2019). Then in 2020, Mhareb et al. reported their research on the glass system $BaO–B_2O_3–SiO_2–TiO_2$ (SC05), or it can be said that he replaced $Bi_2O_3$ in SC01 with $SiO_2$ and $TiO_2$. In that study, $E_g$ was obtained, which was more significant than the use of $Bi_2O_3$, which was equal to 3.36 eV. Then in SC11, Dwaikat et al. (2021) replaced $Bi_2O_3$ in SC01 with $TeO_2$ and SrO to become a $BaO–B_2O_3–TeO_2–SrO$ glass system. The $E_g$ produced by this glass system is 3.00 eV. Furthermore, in 2022, Mhareb et al. observed the optical properties of the $BaO–B_2O_3–TeO_2$ glass system (SC18), the $E_g$ value obtained was 3.46 eV. Based on these results, it can be said that the addition of SrO oxide to the $BaO–B_2O_3–TeO_2$ glass system can reduce its $E_g$.

### 5.4. Shielding properties

Table 1 shows that the material most often combined with BaO to form a glass system for gamma-ray radiation shielding applications is $B_2O_3$. The use of $B_2O_3$ as an admixture in a glass system is due to its low melting point, viscosity, chemical resistance, thermal stability, optical transparency, and mechanical properties (Dwaikat et al., 2021; Singh et al., 2022; Tashlykov et al., 2021; Zakaly et al., 2021). Other materials often combined with BaO are $Bi_2O_3$, $SiO_2$, ZnO, $TeO_2$, and $Na_2O$. The density and radiation shielding properties of the BaO-based glass system experimentally at energy 0.662 MeV can be seen in Table 6. Samples SC01 and SC09, the same $Bi_2O_3–BaO–B_2O_3$ glass system, have different HVL, namely 1.44 and 2.43 cm, respectively. The better ability of SC01 is due to the high composition of $Bi_2O_3$, which plays a role in increasing the density of the sample. Then in 2022, Chinthakayala et al. also observed the effectiveness of the $Bi_2O_3–BaO–B_2O_3$ (SC16) glass system with a lower $Bi_2O_3$ composition than SC01 but an increased amount of BaO. This study showed that the density of SC16 was much greater than that of SC01 and SC09, so it affected a lower HVL. The effectiveness of SC16 as a radiation shield suggests that BaO is a potential material to replace lead-based radiation shields. This statement is supported by the lower HVL SC16 than samples containing PbO, such as SC02, SC04, and SC14. Overall, the comparison of density and HVL of all samples can be seen in Fig. 4.

To get a radiation shield free of lead, it is necessary to study some samples with good shielding effectiveness. Five lead-free samples have been reported to have the lowest HVL values at 0.662 MeV experimentally: SC16, followed by SC15, SC01, SC10, and SC06. Furthermore, several shielding parameters such as total linear attenuation coefficient ($\mu$), total mass attenuation coefficient ($\mu_m$), mean free path (MFP), tenth value layer (TVL), half value layer (HVL), Atomic Cross-Section ($\sigma_{t,a}$), Electronic Cross-Section ($\sigma_{t,el}$), Effective electron density ($N_{eff}$) and Effective atomic number ($Z_{eff}$) theoretically redefined using Phy-X/PSD software with reference to the compositions and densities of the glazing systems are contained inTables 1 and 6.

Fig. 5 shows $\mu$ and $\mu_m$ of the five selected samples at energies of 0.284, 0.347, 0.662, 0.826, 1.173, 1.333, and 2.506 MeV. In Fig. 5 it can be seen that $\mu$ SC16 is larger than SC01 but has a lower $\mu_m$. This is inseparable from that $\rho$ SC16 is much larger than SC01. Then an interesting thing can be seen in Fig. 5b, where at energies of 0.284 and 0.347 MeV, $\mu_m$ SC06 is larger than SC10, but the opposite happens for energies of 0.662–2.506 MeV. Based on the glass composition of SC06 which is dominated by $TeO_2$ and SC10 which is dominated by $B_2O_3$, speculation can arise that at high energy $B_2O_3$ is better than $TeO_2$.

Fig. 6 shows the HVL, TVL, and MFP of samples SC16, SC15, SC01,

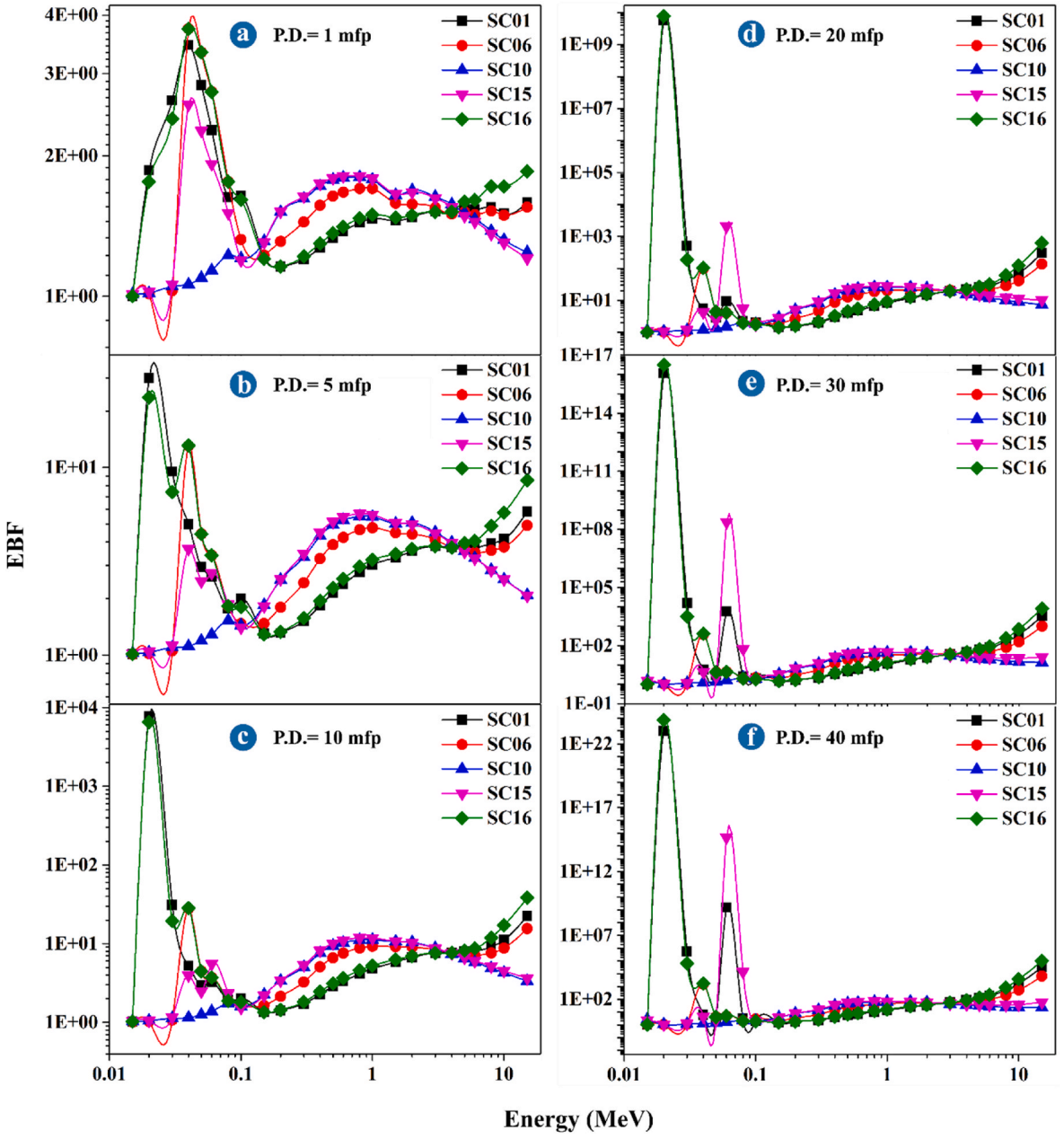


**Fig. 9.** EBF values that depend on photon energy in the range 0.015–15 MeV at different mfp values.

SC10, and SC06 for selected energies from the range 0.284–2.506 MeV. For all selected energies, the order of HVL values from smallest to largest is SC16, SC01, SC06, SC10, and SC15. This sequence is inconsistent with the results obtained experimentally for the energy 0.662 MeV; the lower HVL SC01 and SC06 experimentally may be due to the uneven distribution of the material in the glass sample (Ardiansyah et al., 2022). Then, in Fig. 6a, it can also be seen that at an energy of 0.284 MeV, HVL SC01 and SC16 have a slight difference, but the higher the energy given the difference between the two becomes bigger and even SC01 gets closer to HVL SC06. This indicates that the ability of the SC01 sample decreases drastically at high energy. This trend is in line with the TVL and MFP values shown in Fig. 6b and c. The decrease in shielding ability at high energy is caused by differences in photon interactions that occur, namely: photoelectric absorption, Compton scattering and pair production processes so that photons penetrate the glass system more easily (Ali et al., 2020; Kaur et al., 2019).

Fig. 7 displays the $\sigma_{t,a}$ and $\sigma_{t,el}$ of the five samples. In Fig. 7a it can be seen that for each energy, $\sigma_{t,a}$ SC10 and SC15 are always aligned, which is different from SC01 and SC06. At energies of 0.284 and 0.347 MeV $\sigma_{t,a}$ SC01 is greater than SC06, but the opposite is true for the energy range of 0.662–2.506 MeV. Then based on Fig. 6b, it can be seen that the $\sigma_{t,el}$ values of all samples decreased simultaneously and are getting closer to the same value at high energy which corresponds to the $\mu$ trend in Fig. 5a. This suitability has led to speculation that there is a relationship between $\mu$ and $\sigma_{t,el}$ that makes the two influence each other.

Fig. 8 shows the $N_{eff}$ and $Z_{eff}$ selected samples. Fig. 8a shows $N_{eff}$ SC10 is lower than SC16 at energy 0.284–0.662 MeV but has the same value at energy 0.826 MeV and becomes higher at energy 1.173–2.506 MeV. At an energy of 1333 MeV, $Z_{eff}$ SC10 is the highest among all samples and the second highest at an energy of 2506 MeV after SC01. Then for $Z_{eff}$ in Fig. 8b, it can be seen that $Z_{eff}$ SC06 is in the third highest position at 0.284 and 0.347 MeV energy but is the second highest at 0.662–2.506 MeV. This trend agrees with the $\sigma_{t,a}$, and the trend in Fig. 6a is confirmed by a directly proportional relationship between the

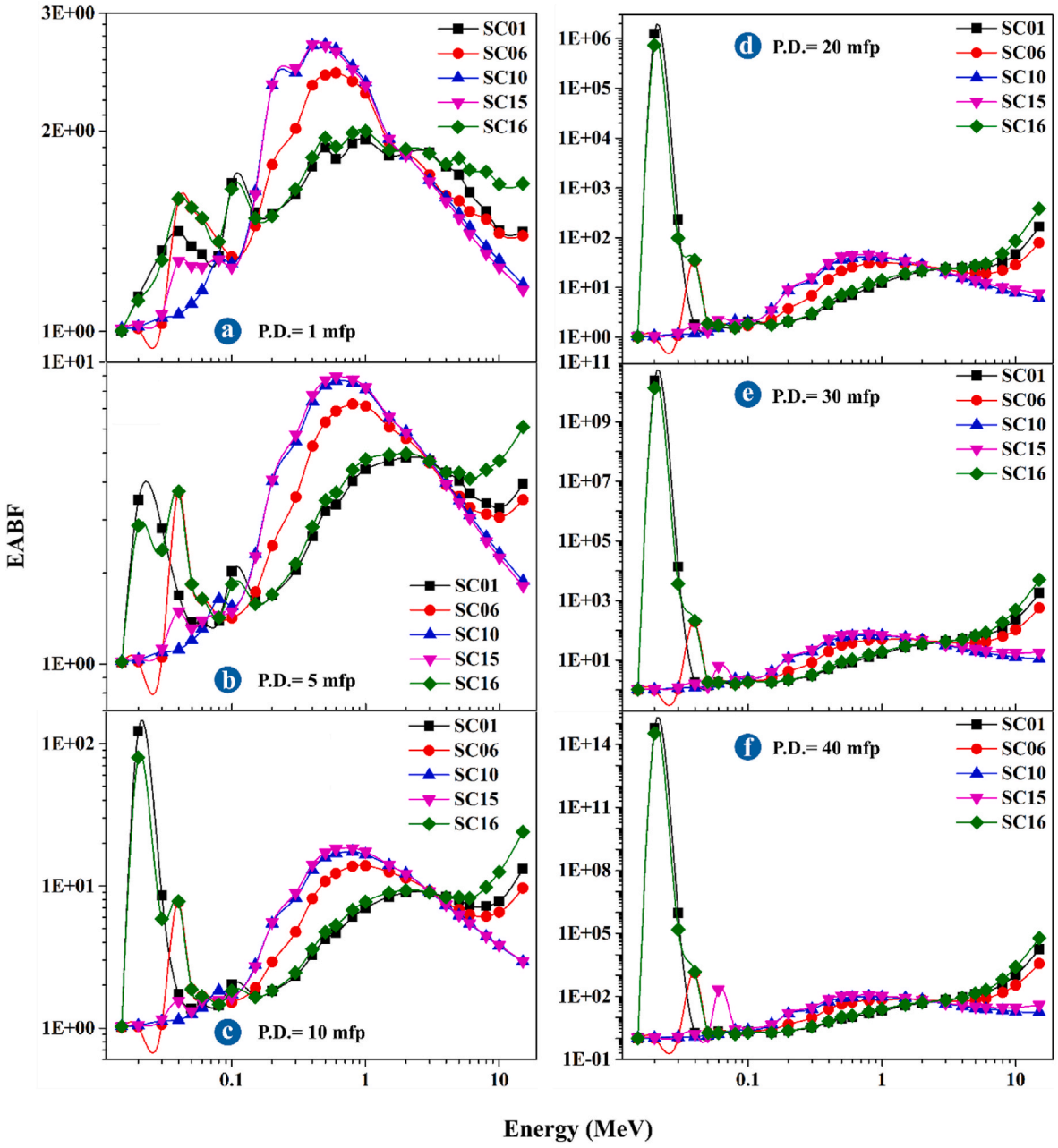


**Fig. 10.** EABF values that depend on photon energy in the range 0.015–15 MeV at different mfp values.

two, which is mathematically presented in equation (35). In Fig. 8b, it can also be seen that $Z_{eff}$ SC06 and SC01 experienced a drastic decrease from 0.347 to 0.662 MeV.

Buildup factors such as EBF and EABF that depend on photon energies several samples at different penetration depth (mfp) are showed in Figs. 9 and 10. The figure shows that the mfp greatly affects EBF and EABF; at the higher mfp, the EBF and EABF also increase. The increase in photon buildup at higher penetration depths occurs because more secondary scattering occurs (El-Mallawany et al., 2020). Figs. 9 and 10 also show that at low energy (especially at a penetration depth of 10–40), SC01 and SC16 have the same trend, and both are higher than SC06, SC10, and SC15. The high buildup factors SC01 and SC16 at low energy indicate that the sample has a greater ability to disperse low-energy photons, and this observation is a major influence of the photoelectric effect (Sabry et al., 2022; Singh et al., 2023).

## 6. Conclusion and future aspect

Barium oxide (BaO) is a metal oxide with the potential as a shield for gamma-ray radiation. After studying 22 recent kinds of literature discussing the use of BaO as one of the compositions of a glass system as a gamma ray radiation shield, it was found that the $Bi_2O_3$–BaO–$B_2O_3$ glass system with sample code SC16 is the sample with the best radiation shielding ability. SC16 has an HVL of 0.937 cm at an energy of 0.662 MeV experimentally, and this value is even better than the glass system containing PbO such as SC02, SC04, and SC14, whose values are only 1.4219, 1.4869, and 1.8810 cm, respectively. After being confirmed in theory using Phy-X/PSD, SC16 is still the best system compared to the others. The quality of the BaO-based glass system as a shield for gamma-ray radiation is also confirmed by its good physical, mechanical, and optical properties.

In order to obtain a BaO-based glass system with better shielding capabilities for gamma-ray radiation, it is necessary to continue

exploring. Some oxide materials that have not been studied too much, such as CaO, $MoO_3$, NaO, $TiO_2$, $H_3BO_3$, $K_2O$, $P_2O_5$, $Dy_2O_3$, CdO, and $V_2O_5$ need to be added to the glass system to observe the effect. Observation of physical, mechanical, and optical properties is also a property that must always be considered in manufacturing BaO-based glass systems.

## Declaration of competing interest

The authors declare that they have no known competing financial interests or personal relationships that could have appeared to influence the work reported in this paper.

## Data availability

Data will be made available on request.

## References


Abd-Allah, W.M., Saudi, H.A., Shaaban, K.S., Farroh, H.A., 2019. Investigation of structural and radiation shielding properties of 40B2O3–30PbO–(30-x) BaO-x ZnO glass system. Appl. Phys. Mater. Sci. Process 125. https://doi.org/10.1007/s00339-019-2574-0.

Abdel-Wahed, M.H., Abdou, S.M., El-Bayoumi, A.S., Salem, S.M., Bendary, A.A., 2020. Structural, optical properties and γ - ray shielding parameters of PbO embedded Li2O borophosphate glass systems. J. Non-Cryst. Solids 543, 120135. https://doi.org/10.1016/J.JNONCRYSOL.2020.120135.

Aboalatta, A., Asad, J., Humaid, M., Musleh, H., Shaat, S.K.K., Ramadan, K., Sayyed, M. I., Alajerami, Y., Aldahoudi, N., 2021. Experimental investigation of zinc sodium borate glass systems containing barium oxide for gamma radiation shielding applications. Nucl. Eng. Technol. 53, 3058–3067. https://doi.org/10.1016/j.net.2021.04.002.

Aboud, H., Aldhuhaibat, M.J.R., Alajermi, Y., 2022. Gamma radiation shielding traits of B2O3–Bi2O3–CdO–BaO–PbO glasses. Radiat. Phys. Chem. 191 https://doi.org/10.1016/j.radphyschem.2021.109836.

Akman, Ferdi, Ogul, H., Ozkan, I., Kaçal, M.R., Agar, O., Polat, H., Dilsiz, K., 2022. Study on gamma radiation attenuation and non-ionizing shielding effectiveness of niobium-reinforced novel polymer composite. Nucl. Eng. Technol. 54, 283–292. https://doi.org/10.1016/j.net.2021.07.006.

Aladailah, M.W., Tashlykov, O.L., Shirmanov, I.A., Strugov, E.D., Sayyed, M.I., Marashdeh, M.W., Elsafi, M., Al-Maaitah, A.F., 2022. Radiation attenuation properties of novel glass system using experimental and Geant4 simulation. Radiat. Phys. Chem. 199 https://doi.org/10.1016/j.radphyschem.2022.110404.

Ali, A.M., Rammah, Y.S., Sayyed, M.I., Somaily, H.H., Algarni, H., Rashad, M., 2020. The impact of lead oxide on the optical and gamma shielding properties of barium borate glasses. Appl. Phys. A 126, 280. https://doi.org/10.1007/s00339-020-3463-2.

Almatari, M., Issa, S.A.M., Dong, M.G., Sayyed, M.I., Ayad, R., 2019. Comparison between MCNP5, Geant4 and experimental data for gamma rays attenuation of PbO–BaO–B2O3 glasses. Heliyon 5. https://doi.org/10.1016/j.heliyon.2019.e02364.

Almurayshid, M., Alsagabi, S., Alssalim, Y., Alotaibi, Z., Almsalam, R., 2021. Feasibility of polymer-based composite materials as radiation shield. Radiat. Phys. Chem. 183, 109425 https://doi.org/10.1016/j.radphyschem.2021.109425.

Aly, P., El-Kheshen, A.A., Abou-Gabal, H., Agamy, S., 2020. Structural investigation and measurement of the shielding effect of borosilicate glass containing PbO, SrO, and BaO against gamma irradiation. J. Phys. Chem. Solid. 145 https://doi.org/10.1016/j.jpcs.2020.109521.

Ardiansyah, A., Rahmat, R., Azlan, M., Heryanto, H., Tahir, D., 2022. Nanocrystal composites cement/BaCO3/Fe2O3 for improved X-ray shielding characteristics: stability structural properties. J. Mater. Res. https://doi.org/10.1557/s43578-022-00775-z.

Ardiansyah, A., Tahir, D., Heryanto, H., Armynah, B., Salah, H., Sulieman, A., Bradley, D. A., 2023. Science mapping for concrete composites as radiation shielding: a review. Radiat. Phys. Chem. 110835 https://doi.org/10.1016/J.RADPHYSCHEM.2023.110835.

Asal, S., Erenturk, S.A., Haciyakupoglu, S., 2021. Bentonite based ceramic materials from a perspective of gamma-ray shielding: preparation, characterization and performance evaluation. Nucl. Eng. Technol. 53, 1634–1641. https://doi.org/10.1016/j.net.2020.11.009.

Aşkin, A., Mutuwong, C., Nutaro, T., Dal, M., 2020. Investigation of the radiation shielding capability of xPbO – (50 - x) BaO – 50 B 2O 3 glass system using Geant4, Fluka, WinXCOM and comparison of data with the experimental data. Pramana - J. Phys. 94 https://doi.org/10.1007/s12043-019-1890-4.

Aşkın, A., Sayyed, M.I., Sharma, A., Dal, M., El-Mallawany, R., Kaçal, M.R., 2019. Investigation ofthe gamma ray shielding parameters of (100-x) [0.5Li2O–0.1B2O3–0.4P2O5]-xTeO2 glasses using Geant4 and FLUKA codes. J. Non-Cryst. Solids 521, 119489. https://doi.org/10.1016/j.jnoncrysol.2019.119489.

Aygün, B., 2020. High alloyed new stainless steel shielding material for gamma and fast neutron radiation. Nucl. Eng. Technol. 52, 647–653. https://doi.org/10.1016/j.net.2019.08.017.

B. Hiremath, G., Hosamani, M.M., Singh, V.P., Ayachit, N.H., M. Badiger, N., 2023. Theoretical investigation of the gamma and neutron interaction parameters of some inorganic scintillators using phy-X/PSD and NGCal software. J. Nucl. Eng. Radiat. Sci. 1–32. https://doi.org/10.1115/1.4056835.

Boonin, K., Yasaka, P., Limkitjaroenporn, P., Rajaramakrishna, R., Askin, A., Sayyed, M. I., Kothan, S., Kaewkhao, J., 2020. Effect of BaO on lead free zinc barium tellurite glass for radiation shielding materials in nuclear application. J. Non-Cryst. Solids 550. https://doi.org/10.1016/j.jnoncrysol.2020.120386.

Chinthakayala, S.K., Gadige, P., Kollipara, V.S., Ramadurai, G., 2022. Gamma radiation shielding studies on highly dense barium bismuth borate glasses. Int. J. Appl. Glass Sci. 13, 211–222. https://doi.org/10.1111/ijag.16554.

Chu, R.D.H., McLaughlin, W.L., Miller, A., Sharpe, P.H.G., 2008. 2. Interactions of electrons and photons with matter. J. ICRU 8, 11–16. https://doi.org/10.1093/jicru_ndn024.

D'Souza, A.N., Sharmila, K., Sayyed, M.I., Somshekarappa, H.M., Khandaker, M.U., Bradley, D.A., Kamath, S.D., 2021. Gamma ray shielding and thermoluminescence investigation of bismuth added heavy metal oxide glasses. Radiat. Phys. Chem. 188 https://doi.org/10.1016/j.radphyschem.2021.109598.

Dwaikat, N., Sayyed, M.I., Mhareb, M.H.A., Dong, M., Alajerami, Y.S.M., Alrammah, I., Khalid, A., Ashiq, M.G.B., 2021. Durability, optical and radiation shielding properties for new series of boro-tellurite glass. Optik 245. https://doi.org/10.1016/j.ijleo.2021.167667.

Echeweozo, E.O., Asiegbu, A.D., Efurumibe, E.L., 2021. Investigation of kaolin - granite composite bricks for gamma radiation shielding. International Journal of Advanced Nuclear Reactor Design and Technology 3, 194–199. https://doi.org/10.1016/j.jandt.2021.09.007.

El-Mallawany, R., Rammah, Y.S., El-Agawany, F.I., Lima, S.M., Mutuwong, C., Al-Buriahi, M.S., 2020. Evaluation of optical features and ionizing radiation shielding competences of TeO2–Li2O (TL) glasses via Geant4 simulation code and Phy-X/PSD program. Opt. Mater. 108, 110394 https://doi.org/10.1016/J.OPTMAT.2020.110394.

El-Mallawany, R., Sidkey, M., Khafagy, A., Afifi, H., 1994. Elastic constants of semiconducting tellurite glasses. Mater. Chem. Phys. 37, 295–298. https://doi.org/10.1016/0254-0584(94)90167-8.

El-Moneim, A.A., Mazen, S.A., Abu-Elsaad, N.I., 2022. Evaluating the theoretical elastic properties of Li-Mn ferrites: a new approach. Mater. Chem. Phys. 291, 126679 https://doi.org/10.1016/J.MATCHEMPHYS.2022.126679.

El-Zaidia, M.M., Ammar, A.A., El-Mallwany, R.A., 1985. Infra-red spectra, electron spin resonance spectra, and density of (TeO2)100−x–(WO3)x and (TeO2)100−x–(ZnCl2)x glasses. Phys. Status Solidi 91, 637–642. https://doi.org/10.1002/pssa.2210910234.

Fidan, M., Acikgoz, A., Demircan, G., Yilmaz, D., Aktas, B., 2022. Optical, structural, physical, and nuclear shielding properties, and albedo parameters of TeO2–BaO–B2O3–PbO–V2O5 glasses. J. Phys. Chem. Solid. 163 https://doi.org/10.1016/j.jpcs.2021.110543.

Geidam, I.G., Matori, K.A., Halimah, M.K., Chan, K.T., Muhammad, F.D., Ishak, M., Umar, S.A., Hamza, A.M., 2022. Optical characterization and polaron radius of Bi2O3 doped silica borotellurite glasses. J. Lumin. 246, 118868 https://doi.org/10.1016/J.JLUMIN.2022.118868.

Gharissah, MuhS., Ardiansyah, A., Pauziah, S.R., Muhammad, N.A., Rahmat, R., Heryanto, H., Tahir, D., 2022. Composites cement/BaSO4/Fe3O4/CuO for improving X-ray absorption characteristics and structural properties. Sci. Rep. 12, 19169 https://doi.org/10.1038/s41598-022-23908-0.

Hampton, R.N., Hong, W., Saunders, G.A., El-Mallawany, R.A., 1988. Dielectric properties of tellurite glass. Phys. Chem. Glasses 29, 100–105.

Hampton, R.N., Hong, W., Saunders, G.A., El-Mallawany, R.A., 1987. The electrical conductivity of pure and binary TeO2 glasses. J. Non-Cryst. Solids 94, 307–314. https://doi.org/10.1016/S0022-3093(87)80066-2.

Hubbell, J.H., 2006. Electron–positron pair production by photons: a historical overview. Radiat. Phys. Chem. 75, 614–623. https://doi.org/10.1016/j.radphyschem.2005.10.008.

Imheidat, M.A., KhHamad, M., Naseer, K.A., Sayyed, M.I., Dwaikat, N., Cornish, K., Alajerami, Y.S., Alqahtani, M., Mhareb, M.H.A., 2022. Radiation shielding, mechanical, optical, and structural properties for tellurite glass samples. Optik 268. https://doi.org/10.1016/j.ijleo.2022.169774.

Kaewkhao, J., Pokaipisit, A., Chewpraditkul, W., 2008. Effect of Bi2O3 content on the properties of Bi2O3-BaO-B2O3 glass system. Adv. Mater. Res. 55–57, 869–872. https://doi.org/10.4028/www.scientific.net/AMR.55-57.869.

Kaur, P., Singh, D., Singh, T., 2016. Heavy metal oxide glasses as gamma rays shielding material. Nucl. Eng. Des. 307, 364–376. https://doi.org/10.1016/J.NUCENGDES.2016.07.029.

Kaur, P., Singh, K.J., Thakur, S., Singh, P., Bajwa, B.S., 2019. Investigation of bismuth borate glass system modified with barium for structural and gamma-ray shielding properties. Spectrochim. Acta Mol. Biomol. Spectrosc. 206, 367–377. https://doi.org/10.1016/j.saa.2018.08.038.

Khazaalah, T.H., Mustafa, I.S., Sayyed, M.I., Rahman, A.A., Zaid, M.H.M., Hisam, R., Malik, M.F.I.A., Ezra, N.S., Naeem, H.S., Khalib, N.C., 2022. Development of novel transparent radiation shielding glasses by BaO doping in waste soda lime silica (SLS) glass. Sustainability 14. https://doi.org/10.3390/su14020937.

Kim, J., Tseren, B., 2020. Occupational ALARA planning for reactor pressure vessel dismantling at kori unit 1. Int. J. Environ. Res. Publ. Health 17, 5346. https://doi.org/10.3390/ijerph17155346.

L'Annunziata, M.F., 2020. The atomic nucleus, nuclear radiation, and the interaction of radiation with matter. In: Handbook of Radioactivity Analysis. Elsevier, pp. 1–243. https://doi.org/10.1016/B978-0-12-814397-1.00001-7.

Levet, A., Özdemir, Y., 2017. Determination of effective atomic numbers, effective electrons numbers, total atomic cross-sections and buildup factor of some compounds for different radiation sources. Radiat. Phys. Chem. 130, 171–176. https://doi.org/10.1016/j.radphyschem.2016.08.015.

Madshal, M.A., El-Damrawi, G., Abdelghany, A.M., Abdelghany, M.I., 2021. Structural studies and physical properties of Gd2O3-doped borate glass. J. Mater. Sci. Mater. Electron. 32, 14642–14653. https://doi.org/10.1007/s10854-021-06022-1.

Mahmoud, K.A., Tashlykov, O.L., Almuqrin, A.H., Sayyed, M.I., Vlasova, S.G., 2022. Assessment of mechanical and radiation shielding capacity for a ternary CdO–BaO–B2O3 glass system: a comprehensive experimental, Monte Carlo simulation, and theoretical studies. Prog. Nucl. Energy 146. https://doi.org/10.1016/j.pnucene.2022.104169.

Mhareb, M.H.A., Alajerami, Y.S.M., Dwaikat, N., Al-Buriahi, M.S., Alqahtani, M., Alshahri, F., Saleh, N., Alonizan, N., Saleh, M.A., Sayyed, M.I., 2021. Investigation of photon, neutron and proton shielding features of H3BO3–ZnO–Na2O–BaO glass system. Nucl. Eng. Technol. 53, 949–959. https://doi.org/10.1016/j.net.2020.07.035.

Mhareb, M.H.A., Alajerami, Y.S.M., Sayyed, M.I., Dwaikat, N., Alqahtani, M., Alshahri, F., Saleh, N., Alonizan, N., Ghrib, T., Al-Dhafar, S.I., 2020. Radiation shielding, structural, physical, and optical properties for a series of borosilicate glass. J. Non-Cryst. Solids 550. https://doi.org/10.1016/j.jnoncrysol.2020.120360.

Mhareb, M.H.A., Alqahtani, M., Alshahri, F., Alajerami, Y.S.M., Saleh, N., Alonizan, N., Sayyed, M.I., Ashiq, M.G.B., Ghrib, T., Al-Dhafar, S.I., Alayed, T., Morsy, M.A., 2020. The impact of barium oxide on physical, structural, optical, and shielding features of sodium zinc borate glass. J. Non-Cryst. Solids 541. https://doi.org/10.1016/j.jnoncrysol.2020.120090.

Mhareb, M.H.A., Sayyed, M.I., Hamad, M.K., Almousa, N., Dwaikat, N., Prabhu, N.S., Monisha, M., Kamath, S.D., 2022. The role of different modifiers on radiation shielding, optical, and physical properties for strontium boro-tellurite glass. Ceram. Int. 48, 15984–15991. https://doi.org/10.1016/j.ceramint.2022.02.141.

Mohammad Rafiei, M., Parsaei, S., Kaur, P., Singh, K.J., Büyükyildiz, M., Kurudirek, M., 2022a. A Monte Carlo investigation of some important radiation parameters and tissue equivalency for photons below 1 keV in human tissues. Biomed Phys Eng Express 8. https://doi.org/10.1088/2057-1976/ac428f.

Mohammad Rafiei, M., Parsaei, S., Kaur, P., Singh, K.J., Büyükyıldız, M., Kurudirek, M., 2022b. Study of low-energy photon interactions below 1 keV for some biological molecules of human body. Eur. Phys. J. E 137. https://doi.org/10.1140/epjp/s13360-022-02445-9.

Muhammad, N.A., Armynah, B., Tahir, D., 2022. High transparent wood composite for effective X-ray shielding applications. Mater. Res. 154, 111930. https://doi.org/10.1016/j.materresbull.2022.111930.

Muramoto, K., Takahashi, Y., Terakado, N., Yamazaki, Y., Suzuki, S., Fujiwara, T., 2018. VO2-dispersed glass: a new class of phase change material. Sci. Rep. 8, 2275. https://doi.org/10.1038/s41598-018-20519-6.

Murray, R.L., Holbert, K.E., 2015. Radiation and materials. In: Nuclear Energy. Elsevier, pp. 71–87. https://doi.org/10.1016/B978-0-12-416654-7.00005-8.

Obodovskiy, I., 2019. Interaction of gamma quanta with matter. Radiation 137–150. https://doi.org/10.1016/B978-0-444-63979-0.00006-9.

Rafiei, M.M., Parsaei, S., Kurudirek, M., 2020. A Monte Carlo study on the gamma-ray buildup factors for the linear sources embedded in a cylindrical shield. J. Instrum. 15 https://doi.org/10.1088/1748-0221/15/11/T11004.

Rafiei, M.M., Tavakoli-Anbaran, H., 2018. Study of exposure buildup factors with detailed physics for cobalt-60 gamma source in water, iron, and lead using the MCNPX code. Eur. Phys. J. E 133. https://doi.org/10.1140/epjp/i2018-12355-8.

Rafiei, Mustafa Mohammad, Tavakoli-Anbaran, H., Kurudirek, M., 2020. A detailed investigation of gamma-ray energy absorption and dose buildup factor for soft tissue and tissue equivalents using Monte Carlo simulation. Radiat. Phys. Chem. 177 https://doi.org/10.1016/j.radphyschem.2020.109118.

Rahmat, R., Halima, N., Heryanto, H., Sesa, E., Tahir, D., 2023. Improvement X-ray radiation shield characteristics of composite cement/Titanium dioxide (TiO2)/Barium carbonate (BaCO3): stability crystal structure and chemical bonding. Radiat. Phys. Chem. 204, 110634 https://doi.org/10.1016/j.radphyschem.2022.110634.

Sabry, N., Yousef, E.S., Alqahtani, M.S., Reben, M., Algarni, H., Umar, A., Albargi, H.B., Yahia, I.S., Zahran, H.Y., 2022. Gamma-ray attenuation properties and fast neutron removal cross-section of Cu2CdSn3S8 and binary sulfide compounds (Cu/Cd/Sn S) using phy-X/PSD software. Radiat. Phys. Chem. 193, 109989 https://doi.org/10.1016/J.RADPHYSCHEM.2022.109989.

Saddeek, Y.B., Aly, K.A., Shaaban, K.S., Ali, A.M., Alqhtani, M.M., Alshehri, A.M., Sayed, M.A., Abdel Wahab, E.A., 2018. Physical properties of B2O3–TeO2–Bi2O3 glass system. J. Non-Cryst. Solids 498, 82–88. https://doi.org/10.1016/j.jnoncrysol.2018.06.002.

Şakar, E., Özpolat, Ö.F., Alım, B., Sayyed, M.I., Kurudirek, M., 2020. Phy-X/PSD: development of a user friendly online software for calculation of parameters relevant to radiation shielding and dosimetry. Radiat. Phys. Chem. 166, 108496 https://doi.org/10.1016/J.RADPHYSCHEM.2019.108496.

Sidkey, M.A., El Mallawany, R.A., Abousehly, A.A., Saddeek, Y.B., 2002. Relaxation of longitudinal ultrasonic waves in some tellurite glasses. Mater. Chem. Phys. 74, 222–229. https://doi.org/10.1016/S0254-0584(01)00466-7.

Singh, J., Kaur, Pardeep, Kaur, Preet, Kumar, V., Singh, K., Singh, T., 2023. Evaluation of radiation shielding parameters of SiO2-Na2O-K2O-P2O5-BaO glass system. Mater. Today: Proc. https://doi.org/10.1016/J.MATPR.2023.03.092.

Singh, J., Kumar, V., Vermani, Y.K., Al-Buriahi, M.S., Alzahrani, J.S., Singh, T., 2021. Fabrication and characterization of barium based bioactive glasses in terms of physical, structural, mechanical and radiation shielding properties. Ceram. Int. 47, 21730–21743. https://doi.org/10.1016/j.ceramint.2021.04.188.

Singh, S., Kaur, R., Rani, S., Sidhu, B.S., 2022. Physical, structural and nuclear radiation shielding behaviour of xBaO-(0.30-x)MgO-0.10Na2O-0.10Al2O3-0.50B2O3 glass matrix. Mater. Chem. Phys. 276 https://doi.org/10.1016/j.matchemphys.2021.125415.

Singh, V.P., Badiger, N.M., 2013. Study of mass attenuation coefficients, effective atomic numbers and electron densities of carbon steel and stainless steels. Radioprotection 48, 431–443. https://doi.org/10.1051/radiopro/2013067.

Singh, V.P., Shirmardi, S.P., Medhat, M.E., Badiger, N.M., 2015. Determination of mass attenuation coefficient for some polymers using Monte Carlo simulation. Vacuum 119, 284–288. https://doi.org/10.1016/j.vacuum.2015.06.006.

Tashlykov, O.L., Sayyed, M.I., Mahmoud, K.A., Khandaker, M.U., Bradley, D.A., Vlasova, S.G., 2021. Tailor made barium borate doped Bi2O3 glass system for radiological protection. Radiat. Phys. Chem. 187 https://doi.org/10.1016/j.radphyschem.2021.109558.

Zakaly, H.M.H., Saudi, H.A., Issa, S.A.M., Rashad, M., Elazaka, A.I., Tekin, H.O., Saddeek, Y.B., 2021. Alteration of optical, structural, mechanical durability and nuclear radiation attenuation properties of barium borosilicate glasses through BaO reinforcement: experimental and numerical analyses. Ceram. Int. 47, 5587–5596. https://doi.org/10.1016/j.ceramint.2020.10.143.